



## Mechanics of self-healing thermoplastic elastomers

Kunhao Yu, An Xin, Zhangzhengrong Feng, Kyung Hoon Lee, Qiming Wang\*

Sonny Astani Department of Civil and Environmental Engineering, University of Southern California, Los Angeles, CA 90089, United States



### ARTICLE INFO

#### Article history:

Received 5 August 2019

Revised 27 November 2019

Accepted 15 December 2019

Available online 23 December 2019

#### Keywords:

Self-healing mechanics

Thermoplastic elastomer

Diffusion-reaction model

Constitutive modeling

Polyurethane

### ABSTRACT

Self-healing polymers crosslinked by dynamic bonds have shown great potential in various engineering applications ranging from electronics to robotics. Due to the intrinsic weakness of dynamic bonds, most of the existing self-healing polymers have relatively weak mechanical strengths. To address this drawback, it is proposed to incorporate crystalline domains within the polymer matrix during the synthesis to make tough and strong self-healing thermoplastic elastomers with semi-crystalline phases. Despite the success in the polymer synthesis, the theoretical understanding of self-healing thermoplastic elastomers remains elusive. In this paper, we develop a theoretical framework to model the constitutive and healing behaviors of self-healable thermoplastic elastomers with both dynamic bonds and semi-crystalline phases. We model the virgin thermoplastic elastomer by using a spring-dash model that couples the soft rubbery phase and the stiff crystalline phase. The rubbery polymer network is formed by layering the body-centered unit cubes that link polymer chains via dynamic bonds. Then, the healing is considered as a coupling of polymer chain diffusion and dynamic-bond binding, leading to an effective diffusion-reaction model. Based on the theoretical framework, we can model the stress-strain behavior of the virgin and healed polymers and theoretically explain the relationship between the healing strength and the healing time. The model can consistently explain our own experiments on self-healable thermoplastic elastomers polyurethane and the documented experiments on self-healable thermoplastic elastomers with disulfide bonds and  $\pi$ - $\pi$  interactions.

© 2019 Elsevier Ltd. All rights reserved.

## 1. Introduction

Self-healing polymers with dynamic bonds have been used in a broad range of engineering applications, such as flexible electronics (Tee et al., 2012), energy storage (Wang et al., 2013b), biomaterials (Brochu et al., 2011), and robotics (Terryn et al., 2017). The healing mechanism primarily relies on the reversible nature of dynamic bonds, i.e., reforming when the fractured materials are contacted. The dynamic bonds include dynamic covalent bonds (Chen et al., 2002; Ghosh and Urban, 2009; Imato et al., 2012; Lu and Guan, 2012; Skene and Lehn, 2004), hydrogen bonds (Chen et al., 2012; Cordier et al., 2008; Montarnal et al., 2009; Phadke et al., 2012; Sijbesma et al., 1997; Wang et al., 2013a), ionic bonds (Das et al., 2015; Haraguchi et al., 2011; Ihsan et al., 2016; Mayumi et al., 2016; Sun et al., 2012; Sun et al., 2013; Wang et al., 2010), metal-ligand coordinations (Burnworth et al., 2011; Holten-Andersen et al., 2011; Kersey et al., 2007; Nakahata et al., 2011; Rowan and Beck, 2005; Wang et al., 2013b), host-guest interactions (Liu et al., 2017a; Liu et al., 2017b), hydrophobic interactions (Gulyuz and Okay, 2014; Okay, 2015), and  $\pi$ - $\pi$  interactions (Fox et al., 2012).

\* Corresponding author.

E-mail address: [qimingw@usc.edu](mailto:qimingw@usc.edu) (Q. Wang).

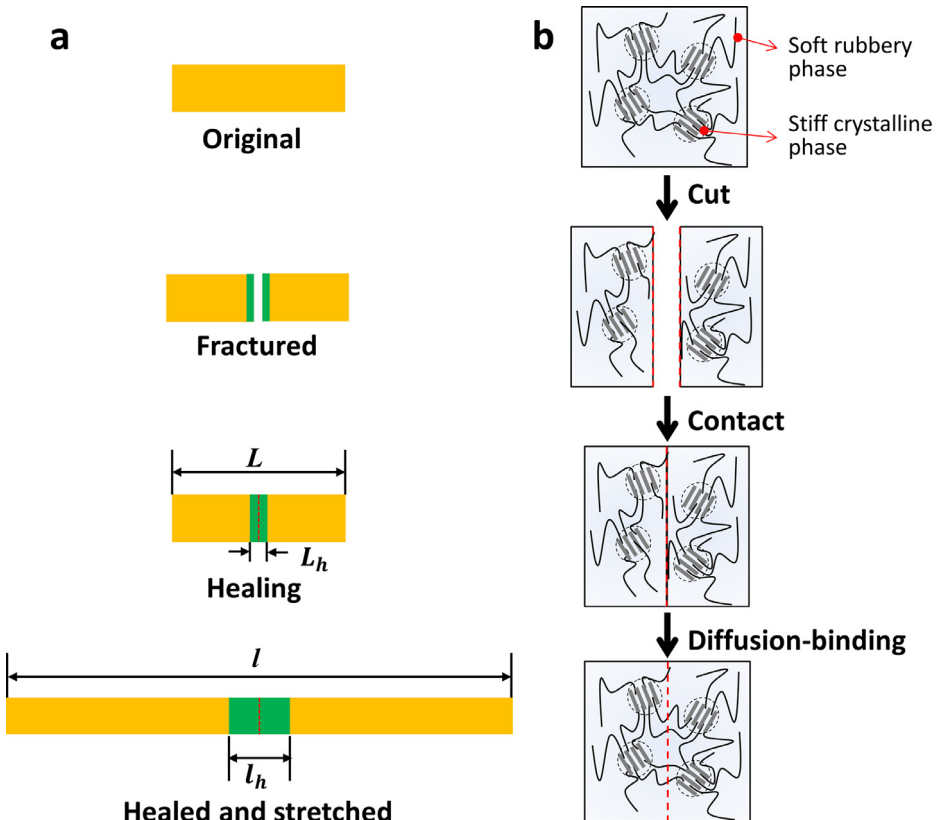


**Fig. 1.** (a) Schematics to show the healing process. (b) Schematics to show the molecular structures around the healing interface during the healing process.

An evident drawback of most of the existing self-healing polymers enabled by dynamic bonds (primarily elastomers and hydrogels) is that their mechanical strengths are typically much weaker than polymers with permanent covalent bonds, because the strength of a dynamic bond is typically much weaker than that of a permanent covalent bond (Chen et al., 2012). To address this drawback, it is proposed to incorporate crystalline domains within the polymer matrix to make tough and strong self-healing thermoplastic elastomers with semi-crystalline phases (Chang et al., 2018; Chen et al., 2012; Ghosh and Urban, 2009; Jian et al., 2018; Ling et al., 2018; Liu et al., 2017c; Xu and Chen, 2016; Zhang et al., 2017). These tough self-healing polymers overcome the low-stiffness-drawback of existing soft self-healing elastomers or hydrogels. Despite the synthesis success, the theoretical understanding of the mechanics of self-healing thermoplastic elastomers has been left behind. The theoretical understanding should include two parts: (1) the modeling of the constitutive behaviors and (2) the modeling of the self-healing behaviors. In the first part, though the constitutive behaviors of the thermoplastic elastomers with permanent covalent bonds have been modeled (Ames et al., 2009; Anand et al., 2009; Boyce et al., 2001; Boyce et al., 1988; Boyce et al., 1989; Cho et al., 2017; Qi and Boyce, 2005), it remains elusive how to understand the constitutive behaviors of the self-healing thermoplastic elastomers with dynamic bonds that can be dissociated by the applied force. In the second part, though we have recently proposed several models to understand the self-healing of self-healable soft polymers in the amorphous state (Wang and Gao, 2016; Wang et al., 2017; Xin et al., 2019; Yu et al., 2018, 2019), it remains elusive how to model the coupling of dynamic bonds, amorphous phase, and crystalline phase within the semi-crystalline polymer network.

Here, we propose a theoretical framework to model the constitutive and self-healing behaviors of self-healable thermoplastic elastomers with both dynamic bonds and crystalline phases. A typical healing experiment is shown in Fig. 1. A thermoplastic elastomer is first cut/broken into two parts, and then immediately brought into contact at a given temperature for a certain period of healing time. The healed sample is then uniaxially stretched until the sample rupture. The tensile stress-strain behavior of the virgin sample will be first modeled by considering both the coupling of the rubbery phase and the crystalline phase and the force-induced dissociation of the dynamic bonds. Then, a diffusion-reaction model will be considered to model the interfacial healing process. Finally, considering the healed sample as a composite with two virgin segments and a small healing segment, we model the stress-strain behavior of the healed sample and then theoretically explain the relationship between the healing strength and the healing time. Effects of the crystallinity fraction, the chain length of the rubbery phase, and the chain mobility on the stress-strain or healing behaviors will be studied. The model can consistently explain our own experiments on self-healable thermoplastic elastomers polyurethane with dynamic disulfide

bonds. The model can also consistently explain others' experimental results on self-healable thermoplastic elastomers with disulfide bonds and  $\pi$ - $\pi$  interactions.

The plan of the paper is as follows: Section 2 introduces our experiments on self-healable polyurethanes. In Section 3, we present the theoretical model system by considering first the constitutive model of the virgin polymer with dynamic bonds, then the interfacial healing process, and finally the stress-strain behavior of the healed polymer. In Section 4, we show the theoretical results for both the virgin and healed polymer. Effects of the crystallinity fraction, the chain length of the rubbery phase and the chain mobility on the stress-strain or healing behaviors will be studied. In Section 5, we will compare our experimental results on the self-healable polyurethanes with the theoretically calculated results. In Section 6, we will use the theoretical model to further explain others' experimental data of self-healable thermoplastic elastomers. The conclusive remarks will be presented in Section 7.

## 2. Experimental

The self-healing thermoplastic elastomers were prepared by preheating 0.00829 mole Polytetramethylene ether glycol (PTMEG, molar mass 250, 1000, and 1810 g/mol) at 90 °C and bubbled with nitrogen for 1 h to remove water and oxygen. 7.369 g isophorone diisocyanate (IPDI), 5 g dimethylacetamide (DMAc) and 0.15 g dibutyltin dilaurate (DBTDL) were mixed with the preheated PTMEG at 70 °C under magnetic stirring for 1 h. Then, a solution with 20 g DMAc and 2.557 g 2-Hydroxyethyl disulfide (HEDS) was added drop-wisely to the mixture with magnetic stirring for another 1 h. To complete the synthesis, 2.147 g 2-Hydroxyethyl methacrylate (HEMA) was mixed with the mixture at 40 °C for 1 h. During the synthesis process, nitrogen was bubbled in the solution to prevent the reaction between the mixture and the oxygen. The obtained solution was put in a vacuum chamber for 12 hours to evaporate 90% of solvent and then mixed with 1 w.t% triethylphosphine (TBP, catalyst), 1 w.t% phenylbis(2,4,6-trimethylbenzoyl)phosphine oxide (photoinitiator) and 0.01~0.02 w.t% Sudan I (photoabsorber) for 2 h. The solution was then used for the projection-based additive manufacturing process to print the thermoplastic elastomer samples. Prepared samples were post-cured for one hour in a UV chamber to enable the full photopolymerization of the material and were heated for 12 h at 40 °C to remove the residual solvent inside the material matrix. Note that all chemicals were purchased from Sigma-Aldrich, USA and were commercially available without further purification.

The prepared strip samples (length 20 mm, width 5 mm, and thickness 1 mm) were first cut into two pieces with a sharp blade and then contact back immediately with clamped on two ends to ensure good contact during the healing process (Fig. 2a). The samples were then healed under 80 °C for various healing time. Note that the glass transition temperatures

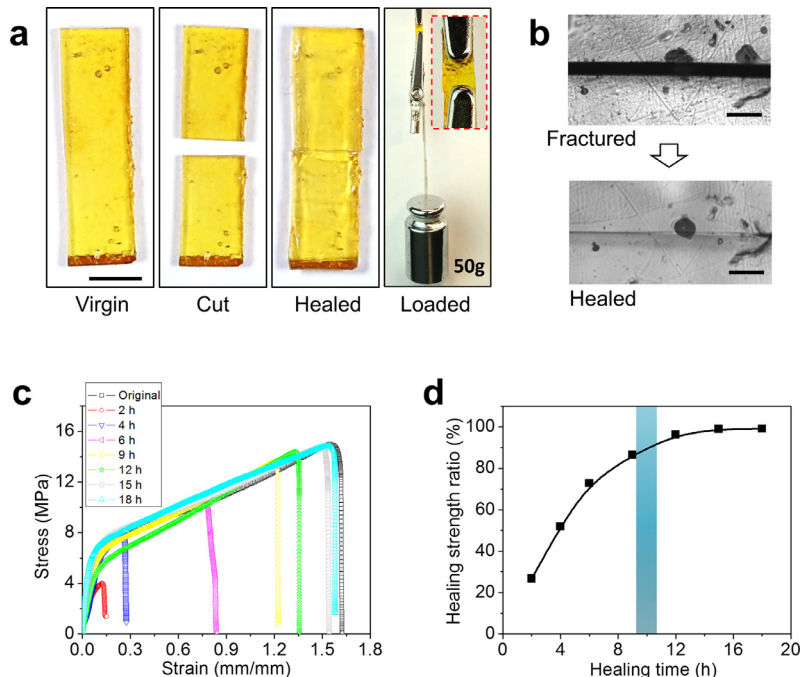


**Fig. 2.** (a) Image sequence to show a self-healing process of a strip polymer sample. The healed sample (0.5 g) can sustain a weight of 200 g. (b) Microscope images to show the fractured and healed interfaces. (c) Tensile stress-strain curves of virgin and healed polymers with various healing time. (d) Healing strength ratios of the healed polymers in functions of the healing time. The healing strength ratio is defined as the tensile strength of the healed polymer normalized by the tensile strength of the virgin polymer. The shadow areas in d indicate the healing time corresponding to 90% healing strength ratio. Scale bars in a represent 4 mm. Scale bars in b represent 300  $\mu$ m.

for polymers with PTMEG 250, 1000, and 1810 g/mol are 65–71 °C, 39 °C, and below 25 °C, respectively (Fig. S1). At 80 °C, all these polymers are in the rubbery state during the healing. The optical microscope (Nikon ECLIPSE LV100ND) was used to monitor the healed surface. The microscopic images show that the fractured interface can be nicely healed during the healing process (Fig. 2b). The healed strip sample can sustain a weight of 50 g that is 200 times its own weight (0.25 g) (Fig. 2a). The mechanical behavior of both virgin and healed samples was tested using Instron (Model 5942) to uniaxially stretch the samples with a strain rate of 0.06 s<sup>-1</sup> until ruptures (Fig. 2c). The tensile stress corresponding to the rupture is considered as the tensile strength of the polymer. The tensile strengths of the self-healed samples for various healing time were normalized by the tensile strength of the virgin sample are calculated as the healing strength ratios, which were then plotted as a function of the healing time (Fig. 2d). On the contrary, the control polymers without disulfide bonds (PTMEG 250 g/mol) could not bond together after the healing experiments at 80 °C for 18 h (Fig. S2).

### 3. Theoretical model

#### 3.1. Overview of the material system

The overall process is shown in Fig. 1a and the molecular structure is modeled as Fig. 1b. We consider that the thermoplastic elastomer is composed of both soft rubbery phase with amorphous polymer chains and stiff crystalline phase with folded polymer segments (Fig. 1b). Effectively, the stiff crystalline phase resembles nanoparticles and each of them bridges a number of polymer chains. Literally, the dynamic bonds can be located within the rubbery phase or crystalline phase. For the sake of analysis simplicity, we here assume that dynamic bonds are only located around the interface between the rubbery phase and the crystalline phase. This assumption can reveal the key physics of the problem, and at the same time significantly reduce the complexity of the problem. Under a sufficiently large force (such as stretching to deform globally and cutting to deform a spot locally), the dynamic bonds between the amorphous chains and the crystalline domain will be forced to broken. When a dynamic bond is broken, it becomes two open distal groups attaching on respective parts. When a sufficiently amount of dynamic bonds are broken, a crack will emerge, or the polymer will be fractured into two pieces. When two fractured pieces are brought into contact with an adequate temperature condition, we assume that the dissociated polymer chain with open distal group will diffuse into the other matrix to find another open distal group to reform the dynamic bond.

#### 3.2. Constitutive model of the virgin thermoplastic elastomer

Following Boyce, Parks, and other authors (Boyce et al., 2001; Boyce et al., 1988; Boyce et al., 1989; Cho et al., 2017; Qi and Boyce, 2005), we employ a spring-dash model to analyze the large-deformation of the thermoplastic elastomer (Fig. 3). The thermoplastic elastomer consists of two phases (Fig. 3a,b): The soft rubbery phase is modeled as nonlinear springs (A and B) and the stiff crystalline phase is modeled as an elastic spring (C) in series with a plastic dash pot (D). To consider the connection between the rubbery phase and the crystalline phase, we consider a general dash-spring model

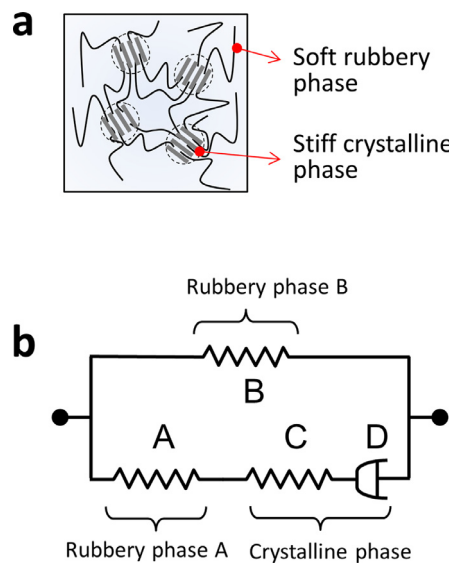


**Fig. 3.** (a) Schematics to show the molecular structure of thermoplastic elastomer. (b) Schematics to show the proposed spring-dash model for the thermoplastic elastomer. A and B are nonlinear springs that present for the soft rubbery phase. C is an elastic spring present for the stiff crystalline phase in series with a plastic dash pot D.

(Fig. 3b). In the model, the rubbery phase is divided into two parts: part A is in series with the crystalline phase C-D, and part B is in parallel with the element A-C-D. The volume fraction of the crystalline phase (CD) within the thermoplastic elastomer matrix is  $P_{CD}$ , and the volume fraction of element A within the rubbery phase is  $\eta_A$ .

The overall deformation gradient of the thermoplastic elastomer  $\mathbf{F}$  can be expressed as

$$\mathbf{F} = \mathbf{F}^B = \mathbf{F}^A \mathbf{F}^{CD} \quad (1)$$

where  $\mathbf{F}^A$ ,  $\mathbf{F}^B$ , and  $\mathbf{F}^{CD}$  are the deformation gradients of elements A, B, and C-D, respectively. According to the schematic layout, the deformation gradient  $\mathbf{F}^{CD}$  can be decomposed into two parts as

$$\mathbf{F}^{CD} = \mathbf{F}^C \mathbf{F}^D \quad (2)$$

where  $\mathbf{F}^C$  and  $\mathbf{F}^D$  are the deformation gradient of the spring element C and the dash pot element D, respectively.

Accordingly, the overall Cauchy stress of the thermoplastic elastomer  $\mathbf{T}$  can be written as

$$\mathbf{T} = \mathbf{T}^B + \mathbf{T}^A = \mathbf{T}^B + \mathbf{T}^{CD} \quad (3)$$

where  $\mathbf{T}^A$ ,  $\mathbf{T}^B$ , and  $\mathbf{T}^{CD}$  are the Cauchy stresses of elements A, B, and C-D, respectively. Due to the in-series configuration, the Cauchy stress of element A and element C-D should be equal, namely,

$$\mathbf{T}^A = \mathbf{T}^{CD} = \mathbf{T}^C = \mathbf{T}^D \quad (4)$$

where  $\mathbf{T}^C$  and  $\mathbf{T}^D$  are the Cauchy stresses of the spring element C and the dash element D, respectively.

### 3.2.1. Rubbery polymer network

Following the essential idea of polymer-network theories (Erman and Mark, 1997; Rubinstein and Colby, 2003; Treloar, 1975), we assume the rubbery polymer network is constructed by layering unit cubes to span over the whole volume (unit cube shown in Fig. 4a). In each unit cube, crystals are located at the corners and centers in a body-centered fashion (Fig. 4a). The corner and center crystals form a crystal pair, and polymer chains with inhomogeneous lengths attach between the crystal pair with dynamic bonds (Fig. 4a). Between a crystal pair, we assume that  $N$  polymer chains are attached (Fig. 4b), each polymer chain made of freely-jointed Kuhn segments with each segment length  $b$  (Erman and Mark, 1997; Rubinstein and Colby, 2003; Treloar, 1975). We assume that the polymer chains can be classified into  $m$  types, each with the same Kuhn number. We denote the Kuhn number (chain length) of the  $i$ th type polymer chain as  $n_i$ , and the number of  $i$ th type chains as  $N_i$ , where  $1 \leq i \leq m$  and  $n_1 \leq n_2 \leq \dots n_i \dots \leq n_m$ . The  $i$ th chain number follows a statistical distribution written as (Fig. 4c)

$$P_i(n_i) = \frac{N_i}{\sum_{i=1}^m N_i} = \frac{N_i}{N} \quad (5)$$

where  $N = \sum_{i=1}^m N_i$  is the total chain number. We here consider a log-normal distribution function as (Wang et al., 2015)

$$P_i(n_i) = \frac{1}{n_i \delta \sqrt{2\pi}} \exp \left[ -\frac{(\ln n_i - \psi)^2}{2\delta^2} \right] \quad (6)$$

where  $\psi$  and  $\delta$  are the mean and standard deviation of  $\ln n_i$ , respectively.  $\psi$  denotes logarithm of the average chain length, and  $\delta$  indicates the chain distribution width.

We then consider the deformation of a single chain, the  $i$ th chain. In the freely-joint state, the average end-to-end distance of the  $i$ th chain is

$$r_i^0 = \sqrt{n_i} b \quad (7)$$

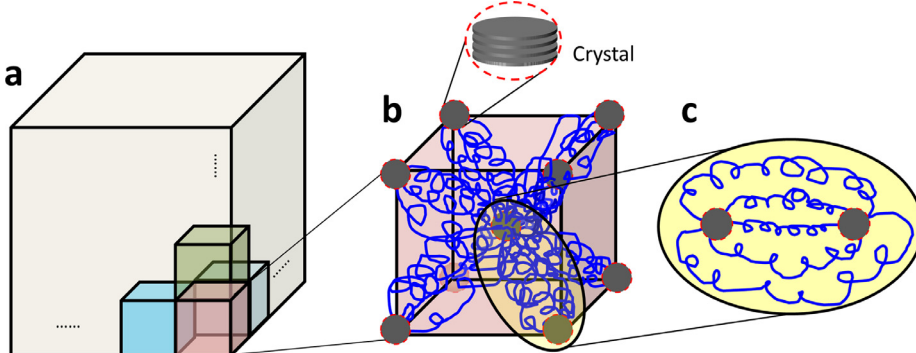


**Fig. 4.** Proposed network model of the thermoplastic elastomer. (a) The polymer consists of layered unit cubes. (b) Crystals are located at the corners and centers in a body-centered fashion. (c) Between a crystal pair, polymer chains with inhomogeneous lengths are attached to the crystal surfaces via dynamic bonds.

Under deformation, the end-to-end distance of the  $i$ th chain becomes  $r_i$ , and the stretch of the  $i$ th chain can be expressed as

$$\Lambda_i = \frac{r_i}{r_i^0} \quad (8)$$

We approximate the end-to-end distance of  $i$ th chain at the fabricated state as the distance between a crystal pair  $L$ , written as,

$$r_i^0 = L \quad (9)$$

The distance between a crystal pair  $L$  can be estimated by using the volume fraction of the crystalline phase  $P_{CD}$ . The volume fraction of the crystalline phase is estimated as

$$P_{CD} = \left( \frac{8\pi d^3}{3} \right) \left/ \left( \frac{2L + 2d}{\sqrt{3}} \right)^3 \right. \quad (10)$$

where  $d$  is the average diameter of the crystalline phase. Using Eq. (10), the crystal pair distance  $L$  is calculated as

$$L = \left[ \left( \frac{\sqrt{3}\pi}{P_{CD}} \right)^{1/3} - 1 \right] d \quad (11)$$

At the deformed state, the rubbery phase has a deformation gradient  $F^A$  or  $F^B$ . We assume that the deformation of the body-centered cube follows the affined deformation assumption (Arruda and Boyce, 1993; Rubinstein and Colby, 2003; Treloar, 1975). Therefore, the distance of the crystal pair at the deformed state becomes

$$r_i = L \sqrt{\frac{I_1}{3}} \quad (12)$$

where the strain invariant  $I_1$  is

$$I_1 = \text{trace}(\mathbf{F}^A \mathbf{F}^{A^T}) \text{ or } \text{trace}(\mathbf{F}^B \mathbf{F}^{B^T}) \quad (13)$$

The stretch of the  $i$ th chain can be calculated as

$$\Lambda_i = \frac{r_i}{\sqrt{n_i b}} = \sqrt{\frac{I_1}{3}} \frac{L}{\sqrt{n_i b}} \quad (14)$$

The chain force on the  $i$ th chain at the current state is

$$f_i = \frac{k_B T}{b} \Gamma^{-1} \left( \frac{r_i}{n_i b} \right) = \frac{k_B T}{b} \Gamma^{-1} \left( \sqrt{\frac{I_1}{3}} \frac{L}{n_i b} \right) \quad (15)$$

where  $\Gamma^{-1}()$  is the inverse Langevin function, and the Langevin function can be written as  $\Gamma(x) = \coth x - 1/x$ .  $k_B$  is Boltzmann constant and  $T$  is the absolute temperature in Kelvin.

For the original material, the initial number of  $i$ th chain per unit material volume is  $N_i$ . This  $i$ th chain density will decrease to  $N_i^a$  as the material deforms because the chain force will motivate the dissociation of the dynamic bond between the chain and the crystal. To model the binding kinetics of the dynamic bond, we denote the reaction from the dissociated state to the associated state as the forward reaction, and otherwise as the reverse reaction. We further denote the associated  $i$ th chain number per unit volume as  $N_i^a$  and the dissociated  $i$ th chain number per unit volume as  $N_i^d$ . The binding reaction kinetics can be written as

$$\frac{dN_i^a}{dt} = k_i^f N_i^d + k_i^r N_i^a \quad (16)$$

where  $k_i^f$  and  $k_i^r$  are forward and reverse reaction rates at the deformed state, respectively. Following the Bell's model, we can write the chain-force-dependent reaction rates as (Bell, 1978; Ribas-Arino and Marx, 2012; Xin et al., 2019; Yu et al., 2018, 2019)

$$k_i^f = k_i^{f0} \exp \left( -\frac{f_i \Delta x}{k_B T} \right) \quad (17)$$

$$k_i^r = k_i^{r0} \exp \left( \frac{f_i \Delta x}{k_B T} \right) \quad (18)$$

If the loading is applied quasi-statically, the active  $i$ th chain volume density  $N_i^a$  can be calculated as a function of the applied chain force,

$$N_i^a = \frac{N_i k_i^{f0} \exp \left( -\frac{f_i \Delta x}{k_B T} \right)}{k_i^{r0} \exp \left( \frac{f_i \Delta x}{k_B T} \right) + k_i^{f0} \exp \left( -\frac{f_i \Delta x}{k_B T} \right)} \quad (19)$$

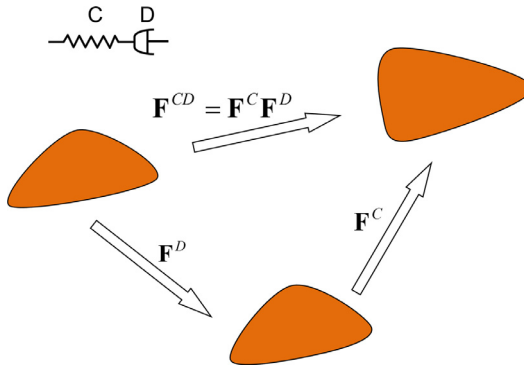


**Fig. 5.** Deformation of the viscoelastic-plastic element in element C and D.

As shown in [Fig. 4](#), one cubic element averagely involves 2 crystals and 8 crystal pairs. The crystal number per unit volume can be estimated as

$$\eta_c = \frac{3P_{CD}}{4\pi d^3} \quad (20)$$

The number of crystal pairs per unit volume is  $4\eta_c$ . Therefore, the free energy density of stretching the polymer network of the deformed original-polymer can be expressed as

$$W_R = \frac{3P_{CD}}{\pi d^3} \sum_{i=1}^m \left( n_i k_B T \left[ \frac{\beta_i}{\tanh \beta_i} + \ln \left( \frac{\beta_i}{\sinh \beta_i} \right) \right] N_i^a \right) \quad (21)$$

where  $\beta_i = \Gamma^{-1}(\Lambda_i / \sqrt{n_i}) = \Gamma^{-1}(\sqrt{I_1/3}L / (n_i b))$ .

### 3.2.2. Visco-elasto-plastic element

The viscoelastic-plastic element is composed of an elastic spring element C and a viscoplastic dash pot element D. The deformation of the two elements can be simply decomposed into two steps: first the plastic flow (element D) and the elastic deformation (element C) ([Fig. 5](#)).

As the plastic flow is incompressible, we have

$$J^D = \det(\mathbf{F}^D) = 1 \quad (22)$$

Therefore, we have

$$J^{CD} = \det(\mathbf{F}^C) \quad (23)$$

The Cauchy stress of C-D element can be calculated as ([Boyce et al., 2001; Boyce et al., 1988; Boyce et al., 1989; Cho et al., 2017; Qi and Boyce, 2005](#))

$$\mathbf{T}^{CD} = \frac{1}{\det(\mathbf{F}^C)} \mathbf{R}^C \mathbf{M}^C \mathbf{R}^C \quad (24)$$

where  $\mathbf{R}^C$  is the rotation tensor that can be obtained through the polar decomposition of the deformation gradient, obtained from

$$\mathbf{F}^C = \mathbf{R}^C \mathbf{U}^C \quad (25)$$

where  $\mathbf{U}^C$  is the elastic stretch tensor. The Mandel stress  $\mathbf{M}^C$  is given by ([Boyce et al., 2001; Boyce et al., 1988; Boyce et al., 1989; Cho et al., 2017; Qi and Boyce, 2005](#))

$$\mathbf{M}^C = \frac{E^C}{(1 + \nu^C)} \ln \mathbf{U}^C + \left( \frac{E^C}{3(1 - 2\nu^C)} - \frac{E^C}{3(1 + \nu^C)} \right) \text{tr}(\ln \mathbf{U}^C) \mathbf{I} \quad (26)$$

where  $E^C$  and  $\nu^C$  are Young's modulus and Poisson's ratio of element C, respectively; and  $\mathbf{I}$  is the identity tensor.

The evolution of the plastic flow is given by

$$\dot{\mathbf{F}}^D = \mathbf{D}^D \mathbf{F}^D \quad (27)$$

where the flow rule is

$$\mathbf{D}^D = \frac{1}{2} \frac{\nu^D}{\bar{\tau}} \mathbf{M}_d^D \quad (28)$$

where  $\mathbf{M}_d^D = \mathbf{M}^C - \text{tr}(\mathbf{M}^C)\mathbf{I}/3$  is the deviator of  $\mathbf{M}^C$ , and the equivalent plastic shear strain rate  $\nu^D$  is modeled as (Boyce et al., 2001; Cho et al., 2017; Qi and Boyce, 2005; Qi et al., 2008)

$$\nu^D = \nu_0 \exp \left[ -\frac{\Delta G_p}{k_B T} \left( 1 - \frac{\bar{\tau}}{Y} \right) \right] \quad (29)$$

And the equivalent shear stress is

$$\bar{\tau} = \sqrt{\frac{1}{2} \mathbf{M}_d^D : \mathbf{M}_d^D} \quad (30)$$

The evolution of the deformation resistance  $Y$  is modeled as

$$\dot{Y} = h(Y_{\text{sat}} - Y)\nu^D \quad (31)$$

where  $Y_{\text{sat}}$  is a saturation level of the deformation resistance.

### 3.2.3. Stress-strain under uniaxial stretch

We assume the rubbery phases are nearly incompressible with the deformation as

$$\det(\mathbf{F}) = \det(\mathbf{F}^B) \approx 1 \quad (32)$$

when the material is under a large-strain uniaxial tension with stretch  $\lambda_1 = \lambda$ , the total deformation gradient can be written as

$$\mathbf{F} = \begin{bmatrix} \lambda & & \\ & \lambda^{-1/2} & \\ & & \lambda^{-1/2} \end{bmatrix} \quad (33)$$

At a given uniaxial stretch  $\lambda$ , we assume the deformation of the element A as

$$\mathbf{F}^A = \begin{bmatrix} \lambda^A & & \\ & \lambda^{A-1/2} & \\ & & \lambda^{A-1/2} \end{bmatrix} \quad (34)$$

The deformation gradient of element C-D is

$$\mathbf{F}^{CD} = \begin{bmatrix} \lambda \lambda^{A-1} & & \\ & \lambda^{-1/2} \lambda^{A-1/2} & \\ & & \lambda^{-1/2} \lambda^{A-1/2} \end{bmatrix} \quad (35)$$

At a given  $\mathbf{F}$ ,  $\mathbf{F}^A$  can be determined by using  $\mathbf{T}^A = \mathbf{T}^{CD}$ , where  $\mathbf{T}^{CD}$  is calculated by Section 3.2.2 using the deformation gradient  $\mathbf{F}^{CD}$ .

When the element B is under a uniaxial tension with  $\mathbf{F}^B = \mathbf{F}$ , the Cauchy stress along the stretching direction can be calculated as

$$T_1^B(\lambda^B) = \frac{3P_{CD}}{\pi d^3} k_B T \frac{L}{b} \left( \lambda^{B2} - \lambda^{B-1} \right) \sum_{i=1}^m \left( \frac{N_i^a \beta_i^B}{\sqrt{3} I_1^B} \right) \quad (36)$$

where  $I_1^B = \text{tr}(\mathbf{F}^B \mathbf{F}^{B^T})$  and  $\beta_i^B = \Gamma^{-1}(L/(n_i b) \sqrt{I_1^B/3})$ .

Combining the Cauchy stress  $\mathbf{T}^B$ , we can obtain the overall Cauchy stress as

$$\mathbf{T} = \mathbf{T}^B + \mathbf{T}^A = \mathbf{T}^B + \mathbf{T}^D \quad (37)$$

which can be written as a function of the deformation gradient  $\mathbf{F}$ . It is expected that the stresses should first increase and then decrease with increasing strains, with a peak point in the middle. In the strain-controlled tensile testing experiment, the peak point is corresponding to a breaking, and the corresponding stress is the tensile strength.

### 3.3. Interfacial self-healing model

The sample is first cut into two parts, and then immediately brought into contact to heal the interface (Fig. 6a). During the cutting process, the dynamic bonds that crosslink the polymer chains in the rubbery elements A and B will be dissociated by the large force induced by the cutting (Fig. 6b). We assume one distal group of the chain is dissociated from a binding site that is within the matrix, and then this distal group will be pulled out of the matrix to the fracture interface. Since the healing experiment is carried out immediately after the cutting, we assume the open distal group on the chain

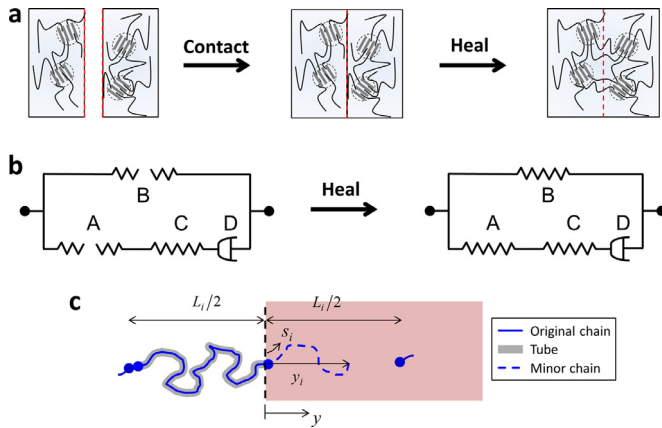


**Fig. 6.** (a) Schematics to show the molecular structures during the healing process. (b) Schematics to show the dissociation and re-association of spring elements during the cutting and healing process, respectively. (c) A schematic to show the diffusion of the  $i$ th polymer chain across the interface.

will still be located around the interface at the very beginning of the healing process, primarily because the migration of the chain and its distal group takes substantial time. During the healing process, the polymer chain with the open distal group will gradually diffuse cross the interface to find the binding site to reform the dynamic bond. Once the dynamic bond is reformed (or re-associated), the polymer chain becomes active and can sustain loading forces.

### 3.3.1. Healing process of the $i$ th chain

The re-binding process of the  $i$ th chain involves the chain diffusion and distal group reaction (Fig. 6c). The radical-assisted binding will facilitate the chain diffusion to cross the healing interface. Therefore, these two processes are strongly coupled.

The chain diffusion can be modeled by following a snake reptation model proposed by De Gennes (De Gennes, 1979; de Gennes, 1971; Doi and Edwards, 1978; Rubinstein and Colby, 2003). The basic idea is that the polymer chain is constrained by the polymer matrix so it can only reptate along a primitive tube (Doi and Edwards, 1988). The primitive tube length is  $L_c$ , so the original chain is divided into  $n_i$  segment with each segment length

$$b_c = \frac{L_c}{n_i} \quad (38)$$

At each small time step, the chain is considered to jump by a step length  $b_c$  in a random-walk fashion. In the original reptation model, the tube length is considered as smaller than the contour length of the  $i$ th chain, i.e.,  $L_c \leq n_i b_c$ ; because the chain may coil around the reptation tube. Subsequently, the jump step  $b_c$  is considered as an unknown parameter. Here, we make a bold assumption that the contour length of the  $i$ th chain is approximately equal to the reptation tube length; therefore, the jump step length

$$b_c \approx b \quad (39)$$

The motion of the polymer chain is enabled by extending out small segments called “minor chains” (Fig. 6c). The curvilinear motion of the polymer chain is characterized by the Rouse friction model with the curvilinear diffusivity of the  $i$ th chain expressed as

$$D_i = \frac{k_B T}{n_i \xi} \quad (40)$$

where  $\xi$  is the Rouse friction coefficient per unit Kuhn segment,  $k_B$  is the Boltzmann constant, and  $T$  is the temperature in Kelvin.

As shown in Fig. 6c, we assume the end-to-end distance of the  $i$ th chain is  $L$ . Without loss of generality, we assume the cutting position is located in the middle of the chain; thus, the distance between the healing interface and the binding site is  $L/2$ . This assumption is just for the sake of analysis simplicity; other location may also work but may involve more complicated statistic averaging algorithm. As shown in Fig. 6c, the distal group will diffuse cross the normal distance  $L/2$  following a curvilinear pathway. To facilitate the analysis, we construct two coordinate systems:  $s$  denotes the curvilinear path along the minor chains, and  $y$  denotes the linear path from the interface to the binding site. When the  $i$ th chain moves  $s_i$  distance along the curvilinear path, it is corresponding to  $y_i$  distance along  $y$  coordinate. Here we assume the selection of the curvilinear path is stochastic in a random-walk fashion (Kim and Wool, 1983; Whitlow and Wool, 1991; Zhang and Wool, 1989). Therefore, the conversion of the distances in two coordinate systems is expressed as (de Gennes, 1971; Doi and Edwards, 1988)

$$y_i = \sqrt{s_i b_c} \approx \sqrt{s_i b} \quad (41)$$

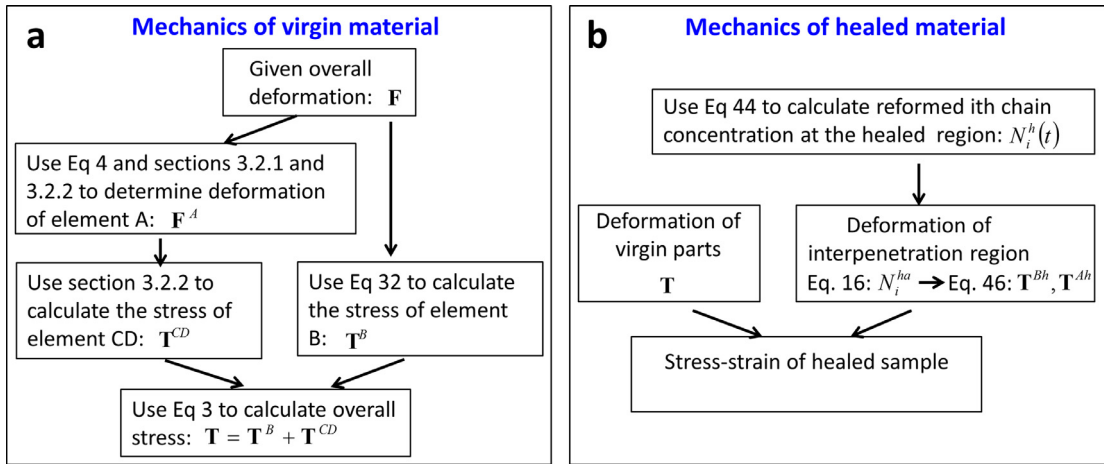


**Fig. 7.** (a) A scheme for calculating the stress-strain behavior of the original polymer. (b) A scheme for calculating the stress-strain behavior of the self-healed polymer sample.

According to Eq. (41),  $L/2$  in the  $y$  coordinate is corresponding to  $L^2/4b$  in the  $s$  coordinate.

The chain diffusion and the association reaction are strongly coupled. We couple the chain diffusion and binding reaction within the region  $0 \leq s \leq L^2/4b$  using an effective diffusion-reaction equation as

$$\frac{\partial C_i^d(s, t)}{\partial t} = D_i \frac{\partial^2 C_i^d(s, t)}{\partial s^2} - \frac{\partial C_i^a}{\partial t} \quad (42a)$$

$$\frac{\partial C_i^a(s, t)}{\partial t} = k_i^{f0} C_i^d(s, t) - k_i^{r0} C_i^a(s, t) \quad (42b)$$

where  $C_i^d(s, t)$  is the inactive  $i$ th chain number per unit length along the curvilinear coordinate  $s$  ( $0 \leq s \leq L^2/4b$ ) at time  $t$  (Fig. 6c), and  $C_i^a(s, t)$  is the corresponding active quantity.  $k_i^{f0}$  and  $k_i^{r0}$  are the forward and the reverse reaction rates at the force-free state, respectively.

At the beginning of the healing process, all mobile open distal groups of the  $i$ th chain are located around the healing interface, which can be expressed as

$$C_i^d(s, t = 0) = N_i \delta(s) \quad (43)$$

$$C_i^a(s, t = 0) = 0 \quad (44)$$

where  $\int_{-\infty}^{\infty} \delta(s) = 1$ .

From Eqs. (42)–(44), we can solve the concentration distributions  $C_i^d(s, t)$  within the curvilinear coordinate. To convert these to the effective concentration of active  $i$ th chain within the region  $0 \leq y \leq L/2$ , we write

$$\frac{N_i^h(t)}{N_i} = 1 - \frac{4b}{L^2} \int_0^{L^2/4b} \frac{C_i^d(s, t)}{N_i} ds \quad (45)$$

where  $N_i^h(t)$  is the average  $i$ th chain number per unit volume of the region  $0 \leq y \leq L/2$  at the undeformed state, and the superscript “ $h$ ” denotes “healed”.

### 3.4. Summary of the model calculation

The healed sample has three segments: one self-healed segment and two original segments (Fig. 1a). The stress-strain behavior of the original segment can be calculated using the scheme shown in Fig. 7a. The stress-strain behavior of the self-healed sample is calculated as follows (Fig. 7b). Under a uniaxial stretch, we consider the deformation gradients of the self-healed segment and the original segments are  $\mathbf{F}^{sh}(\lambda^{sh})$  and  $\mathbf{F}^0(\lambda^0)$ , respectively. As the volume of the self-healed segment is so small, we approximate the overall stretch of the sample  $\lambda^h$  as

$$\lambda^h = \lambda^0 \quad (46)$$

For the self-healed segment with the deformation gradient  $\mathbf{F}^{sh}$ , the deformation gradient of element B as  $\mathbf{F}^{Bh}$ . Under uniaxial stretch  $\lambda^{Bh}$ , the Cauchy stress of the element B

$$T_1^{Bh}(\lambda^{Bh}) = \frac{3P_{CD}}{\pi d^3} k_B T \frac{L}{b} \left( \lambda^{Bh 2} - \lambda^{Bh -1} \right) \sum_{i=1}^m \left( \frac{N_i^{ha} \beta_i^{Bh}}{\sqrt{3} I_1^{Bh}} \right) \quad (47)$$

where  $I_1^{Bh} = \text{tr}(\mathbf{F}^{Bh}\mathbf{F}^{BhT})$  and  $\beta_1^{Bh} = \Gamma^{-1}(L/(n_i b)\sqrt{I_1^{Bh}/3})$ . At a given  $\mathbf{F}^{Sh}$ , we will employ  $\mathbf{T}^{Bh} = \mathbf{T}^A + \mathbf{T}^{CD}$  to determine  $\mathbf{F}^{Bh}$ . Then the overall stress-strain behavior of the healed segment can be determined.

Along the stretching direction, we consider that the Cauchy stress of the self-healed segment and the original segment should be equal, written as

$$T_1^{Bh}(\lambda^{Bh}) = T_1^B(\lambda^{Bo}) \quad (48)$$

where  $T_1^{Bh}(\lambda^{Bh})$  is given by Eq. (47) and  $T_1^B(\lambda^{Bo})$  is given by Eq. (36); and  $\lambda^{Bo}$  is determined using  $\lambda^o$  and Eq. (3). From the above equations, we can eventually calculate the overall stress-strain behavior of the self-healed sample (Fig. 7b).

When the temperature increases from the room temperature to the healing temperature (e.g., 80 °C), the crystalline phase will undergo a phase transition to transfer to the rubbery phase. However, we do not need to consider the phase transition in our modeling system. It is because of the following reasons: (1) We only test the stress-strain behavior of polymers at room temperature, that is, virgin polymers at room temperature and healed polymer at room temperature. The crystalline phase would transfer to the rubbery phase at 80 °C, but will transfer back to the crystalline phase at room temperature. (2) We here assume that only the rubbery phase is fractured before healing (Fig. 6b). Then, during the healing process, only the polymer chains within the rubbery phase interpenetrate into the other matrix.

#### 4. Theoretical results

In this section, we will present the theoretical results calculated from the model presented in Section 3. We will first show the stress-strain behavior of the virgin thermoplastic elastomer and study the effect of the phase fraction on the stress-strain behavior of the virgin material. Then, we will study the stress-strain behavior of the healed material and examine the effects of chain length and chain mobility on the self-healing behavior.

##### 4.1. Stress-strain of the virgin thermoplastic elastomer

We consider the chain length of the soft phase follows a log-normal distribution (Fig. 8a). When the soft phase is loaded, the stress response will first increase to resist the deformation. As the strain increases, the polymer chain is dissociated due to the dissociation of the dynamic bonds. When the strain is sufficiently large, most of the polymer chains are dissociated and the stress response begins to decrease. Therefore, the stress-strain curve first increases and then decreases, featuring a critical maximal point (Fig. 8b). For the stiff phase, we model it using a linear combination of an elastic element C and a viscoplastic dash pot element D. When the strain is small (<0.1), it shows an elastic behavior with a modulus much larger than the soft phase (Fig. 8b). As the strain increases, the stress gradually reaches a plateau with the plastic yielding. Overall, the stress-strain of the self-healable thermoplastic elastomer is presented in Fig. 8c. In the small-strain range (<0.1), the material behaves like an elastic solid. Afterwards, the material undergoes a strain-hardening range with increasing stress as the strain increases. This strain-hardening range is due to the increasing stress of the soft rubbery phase during the plastic yielding of the stiff crystalline phase. When the soft phase reaches the critical maximal point, the overall material also reaches a critical maximal point, which is corresponding to the material rupture under the tensile load. It shows that the material rupture is primarily governed by the failure in the soft phase which is related to the dissociation of the dynamic bonds. This critical maximal stress of the material is the tensile strength of the material. Compared to the existing theoretical model for the thermoplastic elastomers (Boyce et al., 2001; Boyce et al., 1988; Boyce et al., 1989; Cho et al., 2017; Qi and Boyce, 2005), this theoretical model has a special capability in predicting the tensile strength of the material.

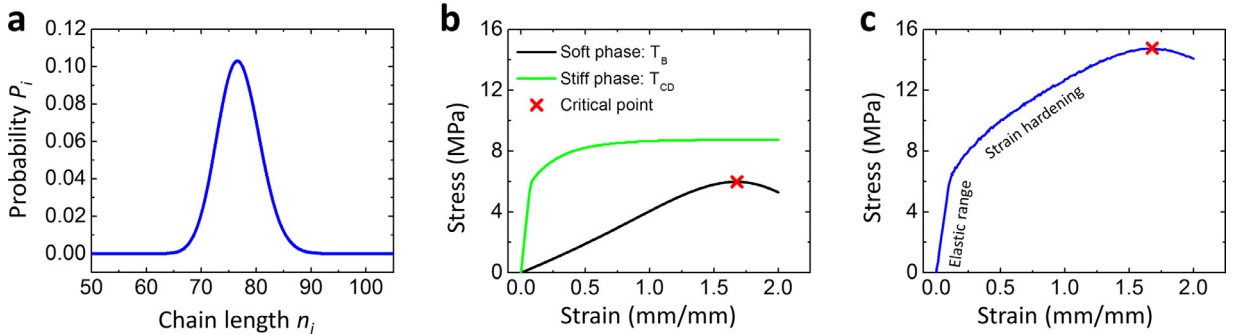
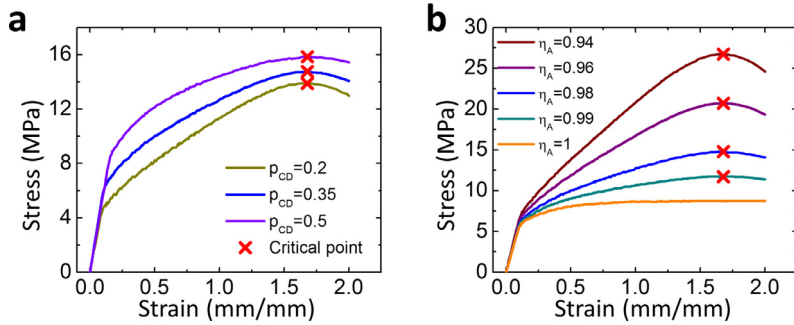


Fig. 8. (a) Probability  $P_i$  in a function of chain length  $n$  for the soft phase. (b) The stress-strain behaviors of the soft phase and stiff phase. (c) The overall stress-strain behavior of the thermoplastic elastomer. The used parameters can be found in Table 1.



**Fig. 9.** Effect of the phase fraction on the stress-strain of the virgin material (a) The theoretically-calculated stress-strain curves of the virgin samples for various crystalline phase volume fraction  $P_{CD}$ . (b) The predicted stress-strain curves of the virgin samples for various volume fraction of element A within the rubbery phase ( $\eta_A$ ). The used parameters can be found in Table 1.

#### 4.2. Effect of phase fraction on the stress-strain of the virgin material

There are two phases within the material matrix: the soft rubbery phase and the stiff crystalline phase. The soft rubbery phase is divided into two parts: element A that is in a series of the crystalline phase CD and element B that is in parallel to elements ACD. First, we maintain the phase fraction between elements A and B and vary the phase fraction of CD to examine the effect of the crystalline phase fraction on the overall stress-strain behavior. As shown in Fig. 9a, as the crystalline phase volume fraction  $P_{CD}$  increases, the yielding stress increases accordingly. However, the elastic modulus, strain-hardening shape, and the critical failure strain only change slightly (or even negligibly). It is because that the plateau stress of the crystalline phase increases as the crystalline phase volume fraction increases; however, the stress-strain shape of the soft rubbery phase does not change. The elastic modulus of the material is primarily governed by the stiffness of the stiff crystalline phase; the strain-hardening shape and failure strain are primarily governed by the soft rubbery phase. When the yielding stress increases but the strain-hardening shape does not change, the tensile strength of the material increases.

Then, we maintain the crystalline volume fraction and vary the volume fraction of element A within the rubbery phase (Fig. 9b). We denote the fraction of element A within the rubbery phase as  $\eta_A$ ; then, the volume fraction of element A within the material matrix is calculated as  $\eta_A(1 - P_{CD})$ . As the element A fraction  $\eta_A$  increases, the strain-hardening range becomes less steep. When  $\eta_A = 1$ , the stress reaches a plateau, resembling the stress-strain behavior of the element CD. The behavior shown in Fig. 9b is because that the strain-hardening shape is primarily governed by the behavior of element B which is in a parallel to elements ACD. As the element A fraction increase, the fraction of element B decreases. When  $\eta_A = 1$ , the model is reduced to only elements ACD, displaying a behavior similar to that of element CD.

#### 4.3. Stress-strain of the healed thermoplastic elastomer

The stress-strain curves of the healed thermoplastic elastomer sample are shown in Fig. 10a. We find that the stress-strain curves of the healed samples follow the path of that of the virgin sample, just featuring lower critical maximal stress points. These critical points are corresponding to the tensile strengths of the healed samples. As the healing time increases, the tensile strengths of the healed sample increases. We denote the healing strength ratio as the tensile strength of the healed sample normalized by that of the virgin sample. We find that the healing strength ratio increases with the increasing time and then reaches a plateau around 100% when the healing time is sufficiently long (Fig. 10b). We define the healing time corresponding to the healing strength ratio of 90% as the equilibrium healing time.

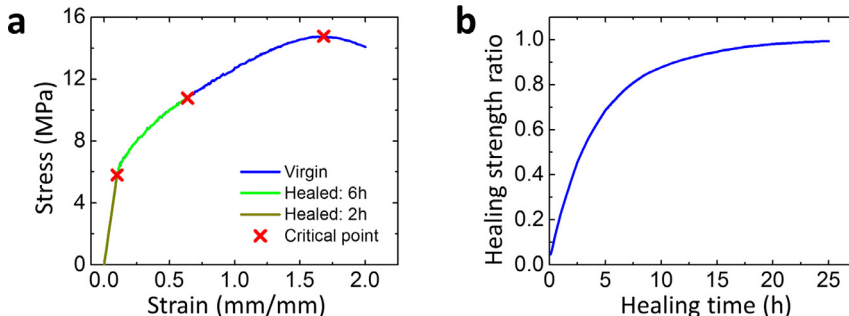


**Fig. 10.** (a) Theoretically-calculated stress-strain curves of the virgin and self-healed thermoplastic elastomer samples under uniaxial tensile strains. (b) Theoretically-calculated healing strength ratio in a function of healing time. The used parameters can be found in Table 1.

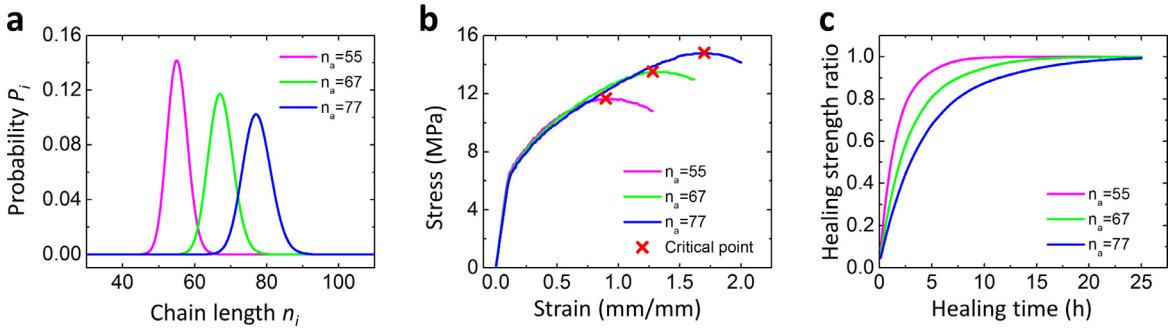


**Fig. 11.** (a) The chain length distributions for various average chain lengths. (b) The predicted stress-strain curves of virgin samples under uniaxial tensile strains. (c) Theoretically-calculated healing strength ratios in functions of healing time. The used parameters can be found in Table 1.

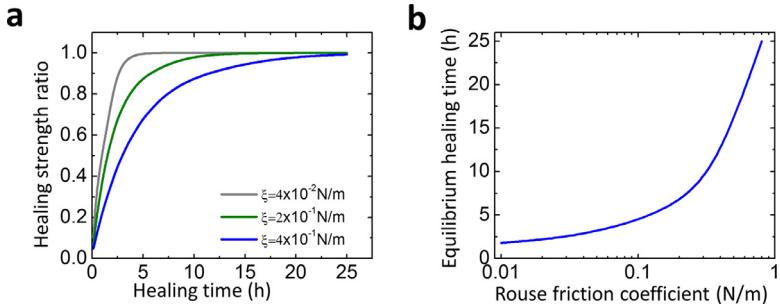


**Fig. 12.** (a) Theoretically-calculated healing strength ratios in functions of healing time for various Rouse friction coefficients  $\xi$ . (b) The predicted equilibrium healing time in a function of the Rouse friction coefficient. The used parameters can be found in Table 1.

#### 4.4. Effect of average chain length of soft rubbery phase

We use a log-normal distribution to capture the chain-length distribution of the rubbery phase (Fig. 11a). As the average chain length  $n_a$  increases, the material becomes more stretchable in the rubbery phase; therefore, the failure strain increases, and the corresponding tensile strength increases (Fig. 11b). At the same time, the chain diffusivity  $D_l$  decreases with the increasing chain length Eq. (40); and the equilibrium healing time to reach 90% healing increases with the increasing chain length.

#### 4.5. Effect of chain mobility

Similarly, if we increase the mobility of the polymer chain alone, the stress-strain behavior of the thermoplastic elastomer does not change, but the healing process requires a shorter time. As shown in Fig. 12ab, the required equilibrium healing time increases with the increasing Rouse friction coefficient  $\xi$ . Because the diffusivity of the polymer chain is in a reverse function of the Rouse friction coefficient  $\xi$ , expressed in Eq. (40).

### 5. Comparison with our own experimental results

After presenting the general characteristics of the theoretically predicted stress-strain behaviors of the virgin and healed thermoplastic elastomers, we compare the theoretical calculations with the experimental results. We first compare the theoretical results with our own experimental results (Fig. 13). The employed parameters and their estimation sources are shown in Table 1. Briefly, the parameters for the rubbery phase and the parameter for the self-healing behavior are estimated based on our previous papers (Wang and Gao, 2016; Wang et al., 2017; Wang et al., 2015; Xin et al., 2019; Yu et al., 2018, 2019). The parameters for the crystalline phase are estimated based on the reported study for the thermoplastic elastomers (Boyce et al., 2001; Boyce et al., 1988; Boyce et al., 1989; Cho et al., 2017; Qi and Boyce, 2005). The volume fraction of the stiff crystalline phase (i.e., crystallinity) is estimated using the differential scanning calorimetry thermographs (Chang et al., 2019; Lin et al., 2019; Motokicho et al., 2013) (Fig. S3). The compositions of the soft rubbery phases A and B are obtained based on curve fitting. We first take a self-healable thermoplastic elastomer with the molar mass of the chain extender PTEMG 1000 g/mol for an example. As shown in Fig. 13a, the theoretically calculated stress-strain behaviors of the virgin and healed thermoplastic elastomers can agree with the experimental counterparts. Likewise, the theoretically calculated healing strength ratio can also consistently match the experimentally measured results (Fig. 13b).

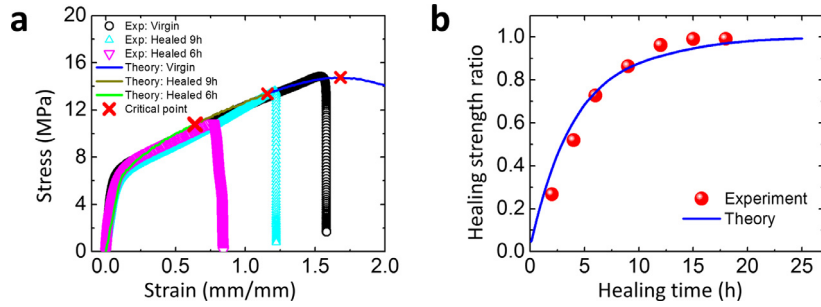


**Fig. 13.** The experimentally-measured and theoretically-calculated (a) stress-strain curves of the original and self-healed samples, and (b) healing strength ratios in a function of the healing time. The used parameters for the theoretical model can be found in Table 1.

**Table 1**

Model parameters used in this paper. The chain dynamics parameters and Rouse friction coefficients are within the reasonable order compared with limited experimental or simulation results in the references (Chapman et al., 1998; Silberstein et al., 2014; Whitlow and Wool, 1991). The parameters for the rubbery phase and the parameter for the self-healing behavior are estimated based on our previous papers (Wang and Gao, 2016; Wang et al., 2017; Wang et al., 2015; Xin et al., 2019; Yu et al., 2018, 2019). The parameters for the crystalline phase are estimated based on the reported study for the thermoplastic elastomers (Boyce et al., 2001; Boyce et al., 1988; Boyce et al., 1989; Cho et al., 2017; Qi and Boyce, 2005). The parameters for the volume fractions of the soft rubbery and stiff crystalline phases are obtained based on curve fitting.

	Parameter	Definition	Figs. 8,10,13	Fig. 9	Fig. 11	Fig. 12	Fig. 14 PU250	Fig. 14 PU 1810	Fig. 15	Fig. 16	Estimation source
Parameters for rubbery phase	$k_i^{f0}$ (s <sup>-1</sup> )	Forward reaction rate	$2 \times 10^{-7}$	$2 \times 10^{-7}$	$2 \times 10^{-7}$	$2 \times 10^{-7}$	$2 \times 10^{-7}$	$2 \times 10^{-7}$	$2 \times 10^{-7}$	$2 \times 10^{-7}$	(Wang and Gao, 2016; Wang et al., 2017; Wang et al., 2015; Xin et al., 2019; Yu et al., 2018, 2019)
	$k_i^{r0}$ (s <sup>-1</sup> )	Reverse reaction rate	$4 \times 10^{-4}$	$4 \times 10^{-4}$	$4 \times 10^{-4}$	$4 \times 10^{-4}$	$4 \times 10^{-4}$	$4 \times 10^{-4}$	$4 \times 10^{-4}$	$3 \times 10^{-4}$	
	$\Delta x$ (m)	Distance along the energy landscape coordinate	$1.4 \times 10^{-9}$	$1.4 \times 10^{-9}$	$1.4 \times 10^{-9}$	$1.4 \times 10^{-9}$	$1.4 \times 10^{-9}$	$1.4 \times 10^{-9}$	$4 \times 10^{-9}$	$4 \times 10^{-9}$	
	$b$ (m)	Kuhn segment length	$5.2 \times 10^{-10}$								
	$n_1$	Minimum chain length	50	50	50	50	13	50	200	200	
	$n_m$	Maximum chain length	200	200	200	200	300	1500	2000	2000	
	$n_a$	Average chain length	77	77	55–77	77	19	96	665	1160	
	$\delta$	Chain length distribution width	0.05	0.05	0.05	0.05	0.1	0.1	0.1	0.15	
Parameters for crystalline phase	$E^C$ (MPa)	Young's modulus of element C	170	170	170	170	1088	74.8	34	4.76	(Boyce et al., 2001; Boyce et al., 1988; Boyce et al., 1989; Cho et al., 2017; Qi and Boyce, 2005)
	$\gamma^C$	Poisson's ratio of element C	0.48	0.48	0.48	0.48	0.48	0.48	0.48	0.48	
	$Y_0$ (MPa)	Initial resistance	6.82	6.82	6.82	6.82	43.6	3	1.36	0.19	
	$Y_{sat}$ (MPa)	Saturated resistance	10.22	10.22	10.22	10.22	65.4	4.5	2	0.29	
	$h$	Hardening modulus	3	3	3	3	3	3	3	3	
	$\Delta G_p/(k_B T)$	Activation energy for plastic deformation	100	100	100	100	100	100	100	100	
Composition parameters	$v_0$	Reference plastic shear rate	0.001	0.001	0.001	0.001	0.001	0.001	0.001	0.001	
	$p_{CD}$	Volume fraction of crystalline phase	0.35	0.2–0.5	0.35	0.35	0.5	0.3	0.35	0.35	Estimated from Fig. S3
	$\eta_A$	Volume fraction of element A in rubbery phase	0.98	0.94–1	0.98	0.98	0.8	0.99	0.992	0.993	Fitting for stress-strain curve
Parameter for self-healing	$\xi$ (N/m)	Rouse friction coefficient	$4 \times 10^{-1}$	$4 \times 10^{-1}$	$4 \times 10^{-1}$	$4 \times 10^{-2} - 13$		$2.6 \times 10^{-1}$	$6.4 \times 10^{-4}$	$5.9 \times 10^{-5}$	Fitting for healing time

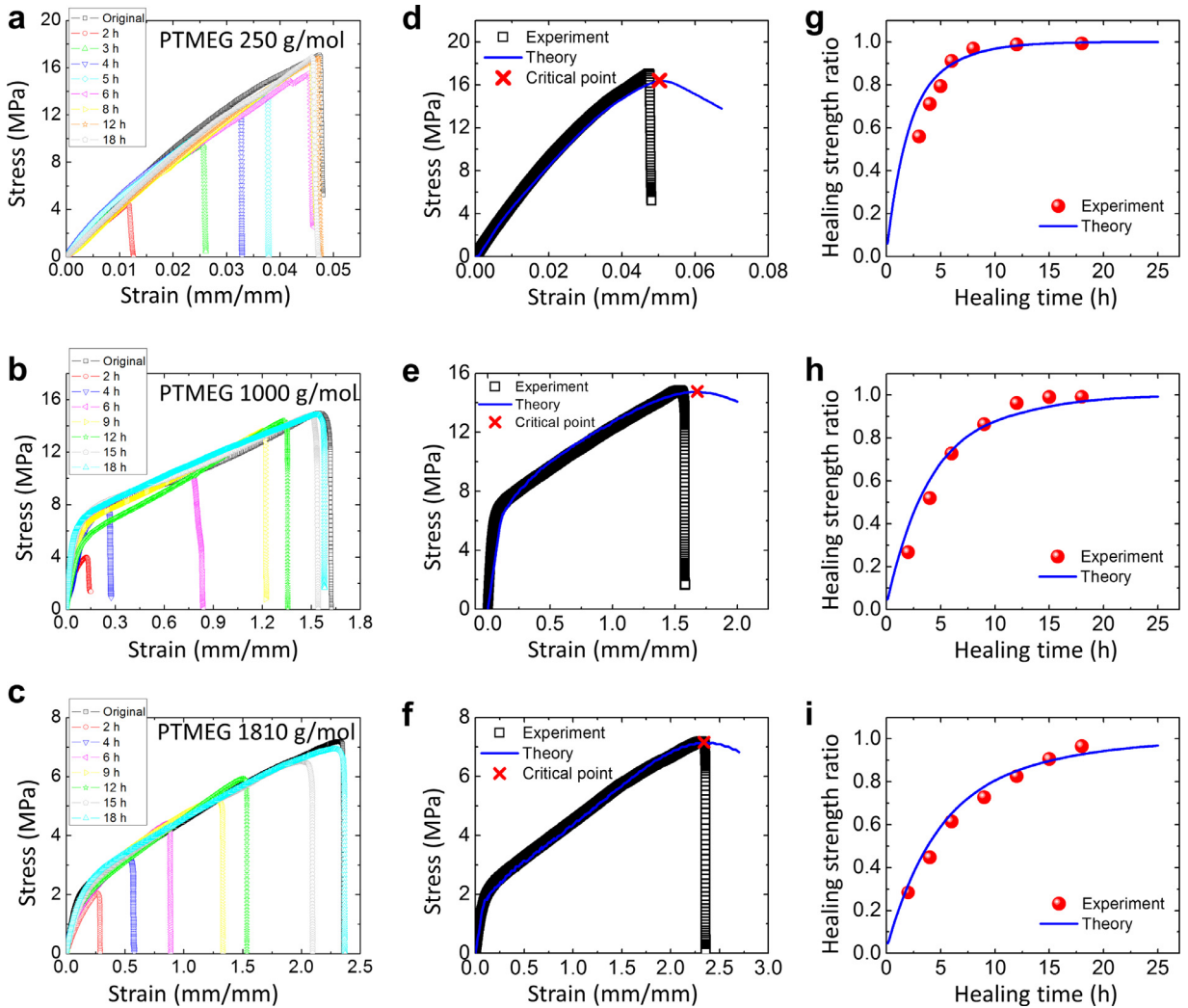


**Fig. 14.** (a-c) Tensile stress-strain curves of the virgin and healed polymers with various healing time. The polymers in a-c have various PTMEG molar masses from 250 to 1810 g/mol, respectively. The experimentally-measured and theoretically-calculated (d-f) stress-strain curves of the original and self-healed samples, and (g-i) healing strength ratios in functions of the healing time. The polymers in d-f and g-i have various PTMEG molar masses corresponding to a-c, respectively. The used parameters for the theoretical model can be found in Table 1.

Then, we vary the molar mass of the chain extender PTMEG from 250 to 1810 g/mol, and the corresponding stress-strain behaviors of the virgin and healed materials are shown in Fig. 14a-c. As the molar mass of the chain extender increases, the volume fraction of the soft rubbery phase increase and gradually dominate the mechanical behavior of the polymer (Fig. 14d-f). In the experiment, the yielding strength and tensile strength of virgin materials decrease as the volume fraction of the rubbery phase increases. This behavior can be theoretically understood based on our model with the effect of phase fraction explained in Section 4. Our theory can quantitatively capture the elastic range, strain hardening and tensile strength of different phase fraction polymers. Also, as the healing time increases, tensile strengths of the healed samples increase until reaching a plateau. The healing strength ratios with various healing time of polymers with different phase compositions can also quantitatively capture by our self-healing model (Fig. 14g-i).

It is also noted that as the rubbery phase volume fraction increases, the equilibrium healing time increases from 6–15 h. This phenomenon can be explained as follows: The healing process is primarily governed by the coupling of diffusion of polymer chains and reforming of dynamic disulfide bonds around the healing interface. Base on the Eq. (40), as the molar mass of the chain extender increases (corresponding to chain length increasing), the diffusivity decreases, and the required healing time is expected to be longer.

## 6. Comparison with others' experimental results

In Section 5, we compare our experimental results on the self-healable polyurethanes with the theoretically calculated results. To further demonstrate the versatility of the present model, we show our model may be applied to understand a

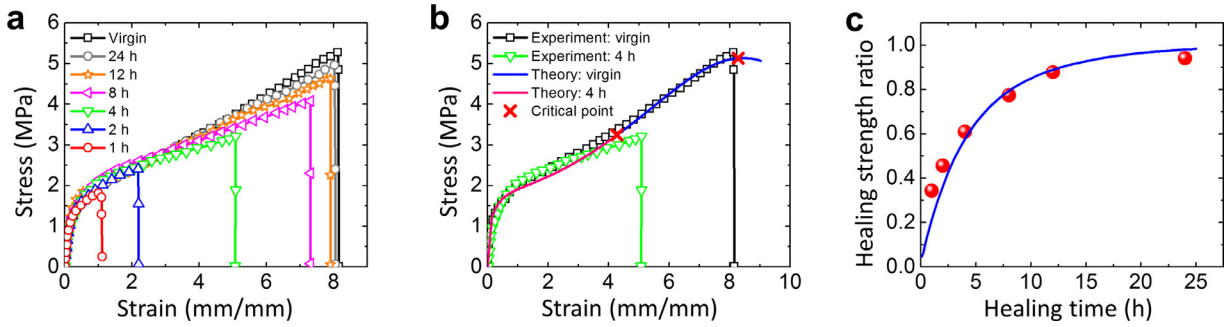


**Fig. 15.** (a) The experimentally-measured stress-strain curves of the original and self-healed samples. The experimentally-measured and theoretically-calculated (b) stress-strain curves of the original and self-healed samples, and (c) healing strength ratios in a function of the healing time. The experimental data in a-c are reproduced from reference (Chang et al., 2018) with permission. The used parameters for the theoretical model can be found in Table 1.

number of thermoplastic polymers with variety of dynamic bonds, including disulfide bonds (Jian et al., 2018; Rekondo et al., 2014; Xu and Chen, 2016), urea bonds (Ying et al., 2014) and hydrogen bonds (Chen et al., 2012). In this section, we will compare the theoretical results with several other's reported experimental results (Chang et al., 2018 and Mei et al., 2016)

### 6.1. Disulfide bonds

The first example is a self-healing polyurethane based on disulfide bonds from 4-4-aminophenyl disulfide (Chang et al., 2018). The disulfide bond is a type of dynamic covalent bond that can trigger the dynamic exchange under elevated temperature. The disulfide bonds were treated as chain-extender introduced in polyurethane prepolymer and exhibited 93.43% healing efficient after being healed for 24 h at 80 °C. The corresponding experimental results are shown in Fig. 15a. Using the presented model, we can use adequate model parameters to consistently explain the experimental stress-strain behavior of original and healed samples (Fig. 15b, parameters in Table 1). In addition, the theoretically calculated healing strength ratio-healing time relationship has a good agreement with the referenced experimental results (Fig. 15c).

### 6.2. $\pi$ - $\pi$ interaction

The second example is a self-healing polymer that crosslinked by Pt $\cdots$ Pt and  $\pi$ - $\pi$  interactions between polydimethylsiloxane (PDMS) and platinum (II) complex (Fig. 16a) (Mei et al., 2016). The dynamic and reversible association-disassociation process of Pt $\cdots$ Pt and  $\pi$ - $\pi$  stacking interactions allow the polymer to realize the self-healing property. The excellent mobility of PDMS chains allows the polymer to heal at room temperature. The healed sample shows the tensile modulus, strength and stretchability can reach more than 90% of those of the original sample after 12 h at room temperature. The corresponding experimental results are shown in Fig. 16b. With adequate parameters, our theoretical model can consistently capture the experimental stress-strain behaviors of the original and healed samples (Fig. 16c). In addition, the healing strength ratios with different healing time from the experiment roughly agree with theoretically calculated results (Fig. 16d). Note that the polymers shown in (Mei et al., 2016) have backbone PDMS chains, but their mechanical behaviors do not necessarily resemble that of the commonly used elastomer PDMS. Actually, the PDMS shown in (Mei et al., 2016) showed an elastoplastic stress-strain curve: a small-strain linear elastic range followed by a strain-hardening region (Fig. 16b).

## 7. Conclusive remarks

In summary, we report a theoretical framework that can explain the constitutive and self-healing behaviors of self-healable thermoplastic elastomers with both dynamic bonds and crystalline phases. We consider the virgin thermoplastic elastomer by employing a general spring-dash model that couples the soft rubbery phase and the stiff crystalline phase. The rubbery polymer network is formed by layering the body-centered unit cubes that link polymer chains via dynamic bonds. During the self-healing process, we use a diffusion-reaction model to model the interfacial healing process. The theoretical framework can explain the stress-strain behaviors of original and self-healed thermoplastic elastomers, as well as the corresponding healing strengths over the healing time. We show that the theoretical framework can nicely explain our own experiments on self-healable thermoplastic elastomers polyurethane with dynamic disulfide bonds and the documented results of thermoplastic materials with disulfide bonds and pi-pi interactions. We expect that our model can be further extended to explain the self-healing behaviors of thermoplastic polymer with a wide range of dynamic bonds (Jian et al., 2018; Rekondo et al., 2014; Xu and Chen, 2016; Ying et al., 2014; Chen et al., 2012).

Note that as an initial attempt to model the self-healing thermoplastic elastomers, we here only focus on the quasistatic loading condition. Actually, the loading rate can affect two aspects of the material behavior: First, the loading rate affects the mechanical behavior of the plastic element D (reference plastic shear rate  $\nu_0$ ). Second, the loading rate also affects the

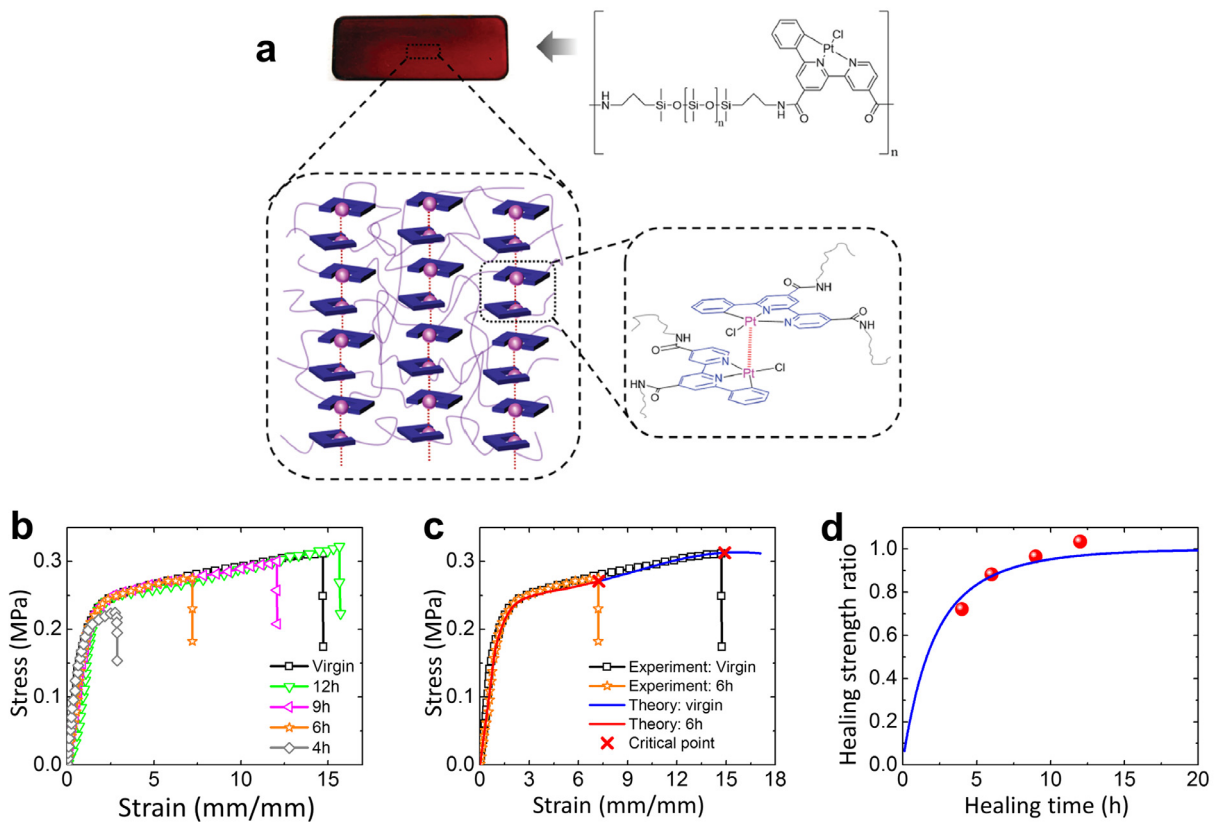


**Fig. 16.** (a) The photograph and proposed structure of the PDMS-Pt film (b) The experimentally-measured stress-strain curves of the original and self-healed samples. The experimentally-measured and theoretically-calculated (c) stress-strain curves of the original and self-healed samples, and (d) healing strength ratios in a function of the healing time. The graph in a and the experimental data in b-d are reproduced from reference (Mei et al., 2016) with permission. The used parameters for the theoretical model can be found in Table 1.

binding kinetics of the dynamic disulfide bonds. We would leave the effect of the loading rate on the mechanical properties of the virgin and healed self-healing thermoplastic elastomers to future research.

In addition, we do not consider the strain-induced crystalline change in our material system. The typical strain-induced crystallinity change is considered in natural rubbers in which the strain can enable the increase of the crystallinity (Dargazany et al., 2014; Guilié et al., 2015; Kroon, 2010; Mistry and Govindjee, 2014; Rastak and Linder, 2018). However, for the polyurethane system, most of the modeling works on polyurethanes have not considered the strain-induced crystallinity change (Boyce et al., 2001; Boyce et al., 1988; Boyce et al., 1989; Cho et al., 2017; Qi and Boyce, 2005).

#### Declaration of Competing Interest

The authors declare that they have no known competing financial interests or personal relationships that could have appeared to influence the work reported in this paper.

The authors declare the following financial interests/personal relationships which may be considered as potential competing interests:

The University of Southern California has filed a patent application related to the self-healing polymers in this work.

#### CRedit authorship contribution statement

**Kunhao Yu:** Conceptualization, Methodology, Formal analysis, Data curation, Writing - original draft, Investigation, Resources. **An Xin:** Investigation, Resources. **Zhangzhengrong Feng:** Investigation, Resources. **Kyung Hoon Lee:** Investigation, Resources. **Qiming Wang:** Conceptualization, Methodology, Formal analysis, Data curation, Writing - original draft, Supervision, Project administration.

#### Acknowledgement

The authors acknowledge the funding support from the National Science Foundation (CMMI-1762567) and the Air Force Office of Scientific Research (FA9550-18-1-0192, program manager: Dr. Jaimie S. Tiley).

## Supplementary materials

Supplementary material associated with this article can be found, in the online version, at doi:[10.1016/j.jmps.2019.103831](https://doi.org/10.1016/j.jmps.2019.103831).

## References

Ames, N.M., Srivastava, V., Chester, S.A., Anand, L., 2009. A thermo-mechanically coupled theory for large deformations of amorphous polymers. Part II: Applications. *Int. J. Plast.* 25, 1495–1539.

Anand, L., Ames, N.M., Srivastava, V., Chester, S.A., 2009. A thermo-mechanically coupled theory for large deformations of amorphous polymers. Part I: Formulation. *Int. J. Plast.* 25, 1474–1494.

Arruda, E.M., Boyce, M.C., 1993. A three-dimensional constitutive model for the large stretch behavior of rubber elastic materials. *J. Mech. Phys. Solids* 41, 389–412.

Bell, G.I., 1978. Models for the specific adhesion of cells to cells. *Science* 200, 618–627.

Boyce, M.C., Kear, K., Socrate, S., Shaw, K., 2001. Deformation of thermoplastic vulcanizates. *J. Mech. Phys. Solids* 49, 1073–1098.

Boyce, M.C., Parks, D.M., Argon, A.S., 1988. Large inelastic deformation of glassy polymers. Part I: rate dependent constitutive model. *Mech. Mater.* 7, 15–33.

Boyce, M.C., Wever, G.G., Parks, D.M., 1989. On the Kinematics of Finite Strain Plasticity. MASSACHUSETTS INST OF TECH CAMBRIDGE.

Brochu, A.B., Craig, S.L., Reichert, W.M., 2011. Self-healing biomaterials. *J. Biomed. Mater. Res. Part A* 96, 492–506.

Burnworth, M., Tang, L., Kumpfer, J.R., Duncan, A.J., Beyer, F.L., Fiore, G.L., Rowan, S.J., Weder, C., 2011. Optically healable supramolecular polymers. *Nature* 472, 334.

Chang, K., Jia, H., Gu, S.-Y., 2018. A Transparent, Highly Stretchable, Self-Healing Polyurethane Based on Disulfide Bonds. *European Polymer Journal*.

Chang, K., Jia, H., Gu, S.-Y., 2019. A transparent, highly stretchable, self-healing polyurethane based on disulfide bonds. *Eur. Polym. J.* 112, 822–831.

Chapman, B.R., Hamersky, M.W., Milhaupt, J.M., Kostecky, C., Lodge, T.P., von Meerwall, E.D., Smith, S.D., 1998. Structure and dynamics of disordered tetrablock copolymers: composition and temperature dependence of local friction. *Macromolecules* 31, 4562–4573.

Chen, X., Dam, M.A., Ono, K., Mal, A., Shen, H., Nutt, S.R., Sheran, K., Wudl, F., 2002. A thermally re-mendable cross-linked polymeric material. *Science* 295, 1698–1702.

Chen, Y., Kushner, A.M., Williams, G.A., Guan, Z., 2012. Multiphase design of autonomic self-healing thermoplastic elastomers. *Nat. Chem.* 4, 467–472.

Cho, H., Mayer, S., Pösel, E., Suosoff, M., in 't Veld, P.J., Rutledge, G.C., Boyce, M.C., 2017. Deformation mechanisms of thermoplastic elastomers: Stress-strain behavior and constitutive modeling. *Polymer* 128, 87–99.

Cordier, P., Tournilhac, F., Soulié-Ziakovic, C., Leibler, L., 2008. Self-healing and thermoreversible rubber from supramolecular assembly. *Nature* 451, 977–980.

Dargazany, R., Khiém, V.N., Itskov, M., 2014. A generalized network decomposition model for the quasi-static inelastic behavior of filled elastomers. *Int. J. Plast.* 63, 94–109.

Das, A., Sallat, A., Böhme, F., Suckow, M., Basu, D., Wießner, S., Stöckelhuber, K.W., Voit, B., Heinrich, G., 2015. Ionic modification turns commercial rubber into a self-healing material. *ACS Appl. Mater. Interfaces* 7, 20623–20630.

De Gennes, P.-G., 1979. *Scaling Concepts in Polymer Physics*. Cornell university press.

de Gennes, P.G., 1971. Reptation of a Polymer Chain in the Presence of Fixed Obstacles. *J. Chem. Phys.* 55, 572–579.

Doi, M., Edwards, S.F., 1978. Dynamics of concentrated polymer systems. Part 1-Brownian motion in the equilibrium state. *J. Chem. Soc. Faraday Trans.* 74, 1789–1801.

Doi, M., Edwards, S.F., 1988. *The Theory of Polymer Dynamics*. Oxford University Press.

Erman, B., Mark, J.E., 1997. *Structures and Properties of Rubberlike Networks*. Oxford University Press, Oxford.

Fox, J., Wie, J.J., Greenland, B.W., Burattini, S., Hayes, W., Colquhoun, H.M., Mackay, M.E., Rowan, S.J., 2012. High-strength, healable, supramolecular polymer nanocomposites. *J. Am. Chem. Soc.* 134, 5362–5368.

Ghosh, B., Urban, M.W., 2009. Self-repairing oxetane-substituted chitosan polyurethane networks. *Science* 323, 1458–1460.

Guilé, J., Le, T.-N., Le Tallec, P., 2015. Micro-sphere model for strain-induced crystallisation and three-dimensional applications. *J. Mech. Phys. Solids* 81, 58–74.

Gulyuz, U., Okay, O., 2014. Self-Healing Poly (acrylic acid) Hydrogels with Shape Memory Behavior of High Mechanical Strength. *Macromolecules* 47, 6889–6899.

Haraguchi, K., Uyama, K., Tanimoto, H., 2011. Self-healing in nanocomposite hydrogels. *Macromol. Rapid Commun.* 32, 1253–1258.

Holten-Andersen, N., Harrington, M.J., Birkedal, H., Lee, B.P., Messersmith, P.B., Lee, K.Y.C., Waite, J.H., 2011. pH-induced metal-ligand cross-links inspired by mussel yield self-healing polymer networks with near-covalent elastic moduli. *Proc. Natl. Acad. Sci. U.S.A.* 108, 2651–2655.

Ihsan, A.B., Sun, T.L., Kurokawa, T., Karobi, S.N., Nakajima, T., Nonoyama, T., Roy, C.K., Luo, F., Gong, J.P., 2016. Self-healing behaviors of tough polyampholyte hydrogels. *Macromolecules* 49, 4245–4252.

Imato, K., Nishihara, M., Kamehara, T., Amamoto, Y., Takahara, A., Otsuka, H., 2012. Self-healing of chemical gels cross-linked by diarylbibenzofuranone-based trigger-free dynamic covalent bonds at room temperature. *Angew. Chem. Int. Ed.* 51, 1138–1142.

Jian, X., Hu, Y., Zhou, W., Xiao, L., 2018. Self-healing polyurethane based on disulfide bond and hydrogen bond. *Polym. Adv. Technol.* 29, 463–469.

Kersey, F.R., Loveless, D.M., Craig, S.L., 2007. A hybrid polymer gel with controlled rates of cross-link rupture and self-repair. *J. R. Soc. Interface* 4, 373–380.

Kim, Y.H., Wool, R.P., 1983. A theory of healing at a polymer-polymer interface. *Macromolecules* 16, 1115–1120.

Kroon, M., 2010. A constitutive model for strain-crystallising Rubber-like materials. *Mech. Mater.* 42, 873–885.

Lin, S., Liu, X., Liu, J., Yuk, H., Loh, H.-C., Parada, G.A., Settens, C., Song, J., Masic, A., McKinley, G.H., 2019. Anti-fatigue-fracture hydrogels. *Sci. Adv.* 5 eaau8528.

Ling, L., Li, J., Zhang, G., Sun, R., Wong, C.-P., 2018. Self-healing and shape memory linear polyurethane based on disulfide linkages with excellent mechanical property. *Macromol. Res.* 26, 365–373.

Liu, J., Tan, C.S.Y., Yu, Z., Lan, Y., Abell, C., Scherman, O.A., 2017a. Biomimetic supramolecular polymer networks exhibiting both toughness and self-recovery. *Adv. Mater.* 29, 1604951.

Liu, J., Tan, C.S.Y., Yu, Z., Li, N., Abell, C., Scherman, O.A., 2017b. Tough supramolecular polymer networks with extreme stretchability and fast room-temperature self-healing. *Adv. Mater.* 29, 1605325.

Liu, W.-X., Zhang, C., Zhang, H., Zhao, N., Yu, Z.-X., Xu, J., 2017c. Oxime-based and catalyst-free dynamic covalent polyurethanes. *J. Am. Chem. Soc.* 139, 8678–8684.

Lu, Y.-X., Guan, Z., 2012. Olefin metathesis for effective polymer healing via dynamic exchange of strong carbon–carbon double bonds. *J. Am. Chem. Soc.* 134, 14226–14231.

Mayumi, K., Guo, J., Narita, T., Hui, C.Y., Creton, C., 2016. Fracture of dual crosslink gels with permanent and transient crosslinks. *Extreme Mech. Lett.* 6, 52–59.

Mei, J.-F., Jia, X.Y., Lai, J.C., Sun, Y., Li, C.H., Wu, J.H., Cao, Y., You, X.Z., Bao, Z., 2016. A highly stretchable and autonomous self-healing polymer based on combination of  $\text{pt}^{***}\text{pt}$  and  $\pi-\pi$  interactions. *Macromol. Rapid Commun.* 37, 1667–1675.

Mistry, S.J., Govindjee, S., 2014. A micro-mechanically based continuum model for strain-induced crystallization in natural rubber. *Int. J. Solids Struct.* 51, 530–539.

Montarnal, D., Tournilhac, F., Hidalgo, M., Couturier, J.-L., Leibler, L., 2009. Versatile one-pot synthesis of supramolecular plastics and self-healing rubbers. *J. Am. Chem. Soc.* 131, 7966–7967.

Motokucho, S., Furukawa, M., Kawashima, M., Kojio, K., Yoshinaga, K., 2013. Physical properties of poly (tetrahydrofuran)-block-poly (2-ethyl-2-oxazoline) triblock copolymer. *Polym. J.* 45, 1115.

Nakahata, M., Takashima, Y., Yamaguchi, H., Harada, A., 2011. Redox-responsive self-healing materials formed from host-guest polymers. *Nat. Comm.* 2, 511.

Okay, O., 2015. Self-healing hydrogels formed via hydrophobic interactions. *Supramol. Polym. Netw. Gels* Springer 101–142.

Phadke, A., Zhang, C., Arman, B., Hsu, C.-C., Mashelkar, R.A., Lele, A.K., Tauber, M.J., Arya, G., Varghese, S., 2012. Rapid self-healing hydrogels. *Proc. Natl. Acad. Sci. U.S.A.* 109, 4383–4388.

Qi, H.J., Boyce, M.C., 2005. Stress-strain behavior of thermoplastic polyurethanes. *Mech. Mater.* 37, 817–839.

Qi, H.J., Nguyen, T.D., Castro, F., Yakacki, C.M., Shandas, R., 2008. Finite deformation thermo-mechanical behavior of thermally induced shape memory polymers. *J. Mech. Phys. Solids* 56, 1730–1751.

Rastak, R., Linder, C., 2018. A non-affine micro-macro approach to strain-crystallizing rubber-like materials. *J. Mech. Phys. Solids* 111, 67–99.

Rekondo, A., Martin, R., de Luzuriaga, A.R., Cabañero, G., Grande, H.J., Odriozola, I., 2014. Catalyst-free room-temperature self-healing elastomers based on aromatic disulfide metathesis. *Mater. Horizons* 1, 237–240.

Ribas-Arino, J., Marx, D., 2012. Covalent mechanochemistry: theoretical concepts and computational tools with applications to molecular nanomechanics. *Chem. Rev.* 112, 5412–5487.

Rowan, S.J., Beck, J.B., 2005. Metal-ligand induced supramolecular polymerization: a route to responsive materials. *Faraday Discuss.* 128, 43–53.

Rubinstein, M., Colby, R., 2003. *Polymer Physics*. Oxford University Press, Oxford.

Sijbesma, R.P., Beijer, F.H., Brunsved, L., Folmer, B.J., Hirschberg, J.K., Lange, R.F., Lowe, J.K., Meijer, E., 1997. Reversible polymers formed from self-complementary monomers using quadruple hydrogen bonding. *Science* 278, 1601–1604.

Silberstein, M.N., Cremar, L.D., Beiermann, B.A., Kramer, S.B., Martinez, T.J., White, S.R., Sottos, N.R., 2014. Modeling mechanophore activation within a viscous rubbery network. *J. Mech. Phys. Solids* 63, 141–153.

Skene, W.G., Lehn, J.-M.P., 2004. Dynamers: polyacylhydrazone reversible covalent polymers, component exchange, and constitutional diversity. *Proc. Natl. Acad. Sci. U.S.A.* 101, 8270–8275.

Sun, J.-Y., Zhao, X., Illeperuma, W.R., Chaudhuri, O., Oh, K.H., Mooney, D.J., Vlassak, J.J., Suo, Z., 2012. Highly stretchable and tough hydrogels. *Nature* 489, 133–136.

Sun, T.L., Kurokawa, T., Kuroda, S., Ihsan, A.B., Akasaki, T., Sato, K., Haque, M.A., Nakajima, T., Gong, J.P., 2013. Physical hydrogels composed of polyampholytes demonstrate high toughness and viscoelasticity. *Nat. Mater.* 12, 932–937.

Tee, B.C., Wang, C., Allen, R., Bao, Z., 2012. An electrically and mechanically self-healing composite with pressure-and flexion-sensitive properties for electronic skin applications. *Nat. Nanotechnol.* 7, 825–832.

Terryn, S., Brancart, J., Lefevere, D., Van Assche, G., Vanderborght, B., 2017. Self-healing soft pneumatic robots. *Sci. Robot.* 2 eaan4268.

Treloar, L.R.G., 1975. *The Physics of Rubber Elasticity*. Oxford University Press, Oxford.

Wang, C., Liu, N., Allen, R., Tok, J.B.H., Wu, Y., Zhang, F., Chen, Y., Bao, Z., 2013a. A rapid and efficient self-healing thermo-reversible elastomer crosslinked with graphene oxide. *Adv. Mater.* 25, 5785–5790.

Wang, C., Wu, H., Chen, Z., McDowell, M.T., Cui, Y., Bao, Z., 2013b. Self-healing chemistry enables the stable operation of silicon microparticle anodes for high-energy lithium-ion batteries. *Nat. Chem.* 5, 1042–1048.

Wang, Q., Gao, Z., 2016. A constitutive model of nanocomposite hydrogels with nanoparticle crosslinkers. *J. Mech. Phys. Solids* 94, 127–147.

Wang, Q., Gao, Z., Yu, K., 2017. Interfacial self-healing of nanocomposite hydrogels: Theory and experiment. *J. Mech. Phys. Solids* 109, 288–306.

Wang, Q., Gossweiler, G.R., Craig, S.L., Zhao, X., 2015. Mechanics of mechanochemically responsive Elastomers. *J. Mech. Phys. Solids* 82, 320–344.

Wang, Q., Mynar, J.L., Yoshida, M., Lee, E., Lee, M., Okuro, K., Kinbara, K., Aida, T., 2010. High-water-content mouldable hydrogels by mixing clay and a dendritic molecular binder. *Nature* 463, 339–343.

Whitlow, S.J., Wool, R.P., 1991. Diffusion of polymers at interfaces: a secondary ion mass spectroscopy study. *Macromolecules* 24, 5926–5938.

Xin, A., Zhang, R., Yu, K., Wang, Q., 2019. Mechanics of electrophoresis-induced reversible hydrogel adhesion. *J. Mech. Phys. Solids* 125, 1–21.

Xu, Y., Chen, D., 2016. A novel self-healing polyurethane based on disulfide bonds. *Macromol. Chem. Phys.* 217, 1191–1196.

Ying, H., Zhang, Y., Cheng, J., 2014. Dynamic urea bond for the design of reversible and self-healing polymers. *Nat. Commun.* 5, 3218.

Yu, K., Xin, A., Wang, Q., 2018. Mechanics of self-healing polymer networks crosslinked by dynamic bonds. *J. Mech. Phys. Solids* 121, 409–431.

Yu, K., Xin, A., Wang, Q., 2019. Mechanics of light-activated self-healing polymer networks. *J. Mech. Phys. Solids* 124, 643–662.

Zhang, H., Wool, R.P., 1989. Concentration profile for a polymer-polymer interface. 1. Identical chemical composition and molecular weight. *Macromolecules* 22, 3018–3021.

Zhang, L., Chen, L., Rowan, S.J., 2017. Trapping dynamic disulfide bonds in the hard segments of thermoplastic polyurethane elastomers. *Macromol. Chem. Phys.* 218, 1600320.